Alkyne-Protected AuPd Alloy Nanoparticles for Electrocatalytic Reduction of Oxygen

Christopher P. Deming,[a] Albert Zhao,[b] Yang Song,[a] Ke Liu,[a] Mohammad M. Khan,[a] Veronica M. Yates,[a] and Shaowei Chen*[a]

Dodecyne-capped AuPd alloy nanoparticles of varying compositions were prepared through the co-reduction of metal-salt precursors with NaBH$_4$. TEM measurements showed that the particles were largely in the range of 2–6 nm in diameter. XPS studies showed that the atomic Pd concentration varied from 65 to 100%. Infrared spectroscopic measurements confirmed the bonding attachment of the dodecyne ligands on the nanoparticle surfaces, which rendered the nanoparticles readily dispersible in common organic media. Electrochemically, the resulting nanoparticles exhibited apparent catalytic activity in oxygen reduction with a volcano-shaped variation with the metal composition. The best performance was identified with the sample composed of 91.2 at% Pd that exhibited a mass activity over eight times better than that of commercial palladium black, and almost twice as good in terms of specific activity. This remarkable performance was accounted for by both alloying with gold and surface functionalization with alkyne ligands that manipulated the electronic interactions between palladium and oxygen species.

1. Introduction

Proton exchange membrane fuel cells (PEMFCs) have been gaining much attention recently as long-range energy sources for commercial vehicles, owing to their fast startup, high energy density, renewable fuel, and environmentally friendly reaction products.[1–3] This technology has provided over 300 miles of car travel, but is not currently available in commercial settings, because a large amount of the catalyst is required for sufficient power output.[1] This large electrocatalytic demand is largely a result of the sluggish electron-transfer kinetics of oxygen reduction reactions (ORRs) at the cathode.[4–6] For electrocatalytic oxygen reduction, platinum has been identified as the optimal single metal, owing to the high catalytic activity and stability under very acidic and strongly oxidizing conditions. Unfortunately, the low abundance and high cost of platinum have limited the scale of such electrocatalyzed fuel cells and, thus, the availability of this energy source for commercial settings, even with the large surface area to volume ratio of nanoparticles.

It is clear that a modified approach must be pursued. In fact, a number of strategies have been developed and described in the literature.[7–16] One effective procedure is to alloy platinum with another metal in the form of homogenous or core–shell structures, which has allowed a drastic decrease in the amount of platinum with equal or better activity than that of pure Pt.[8–11, 17] This enhancement in activity is attributed to the electronic interactions between neighboring atoms as well as strains from lattice mismatch.[10, 11] These effects are respectively termed ligand and strain effects and alter the catalytic activity based on changes in the adsorption kinetics of oxygen on the nanoparticle surface.[18–21] For instance, previous studies have shown that the activity of Pt(111) surfaces modified with a subsurface copper layer exhibits a volcano-shaped trend when plotted versus the content of copper.[22] Generally, platinum and platinum-group metals bind too strongly to oxygenated intermediates. The trend in activity is, therefore, a result of weakening interactions of oxygenated intermediates with the platinum surface as copper content increases, with the peak representing the optimal concentration: low copper contents lead to strong interactions with oxygen, resulting in unfavorable removal of the final products and a small number of active sites, whereas high copper contents result in unfavorable initial adsorption and, thus, a low number of surface oxygen groups to reduce. This volcano trend was predicted by Sabatier years ago, with the peak activity in agreement with theoretical calculations based on adsorption energies.[23]

The enhancement in electrocatalytic activity of alloys, as compared to pure metal constituents, has also been recognized for many non-platinum metals including gold and palladium.[20, 21, 24–32] For instance, palladium is a platinum-group metal that binds to oxygen even more strongly than platinum, whereas gold has very little interaction with oxygen, making these two metals optimal candidates for a binary alloy.[23] The electrocatalytic properties of AuPd alloy nanoparticles have been found to be largely dependent on the size, elemental

[a] C. P. Deming, Y. Song, K. Liu, M. M. Khan, V. M. Yates, Prof. Dr. S. Chen
Department of Chemistry and Biochemistry
University of California
1156 High Street, Santa Cruz, CA 95064 (USA)
E-mail: shaowei@ucsc.edu

[b] A. Zhao
The Harker School
4300 Bucknell Road, San Jose, CA 95130 (USA)

composition, and distribution; thus, much effort has been focused on controlling such features.[33] For instance, stabilization and reduction in sol-gel has afforded monodispersed AuPd particles with diameters between 2.0 and 7.5 nm, which have exhibited onset potentials at least 200 mV more positive for oxygen reduction than a bare glassy-carbon electrode.[34] Ionic liquid microemulsion techniques have enabled precise control over the elemental composition[35] in addition to allowing for temporal separation between reduction of metals and, consequently, control over elemental distribution.[36] Co-reduction of metal salts in alcohols has yielded alloy particles with a gold-enriched core and palladium-enriched shell with an average particle diameter of 2.14 nm.[37] Intermittent microwave heating combined with sodium borohydride reduction produced gold palladium alloy nanoparticles supported on tungsten carbide, which exhibited an onset potential for oxygen reduction 70 mV more positive than that of commercial platinum electrocatalysts.[24] From these studies, it is clear that gold and palladium alloys offer promising results; yet, the optimal ratio of gold and palladium in nanoparticles for electrocatalytic oxygen reduction has remained largely unexplored, to the best of our knowledge. This is the primary motivation and focus of the present work.

Another method to alter the adsorption kinetics of oxygenated species and, thus, the electrocatalytic activity is the choice of capping ligands.[12–16] Organic ligands can protect metals from dissolution in addition to providing modifications of the electronic surface structure. In recent studies, we have shown that platinum nanoparticles might be functionalized with acetylene derivatives and exhibit apparent electrocatalytic activity in oxygen reduction.[12] It was found that the activity varied largely with the capping ligands, where the discrepancy was attributed to electronic interactions of the metal cores with the ligands that strongly influence the binding interaction to oxygenated intermediates. In another study,[16] we functionalized silver nanoparticles with 1-hexanethiol, 1-octyne, and 4-trifluoromethylphenyl ligands and examined their electrocatalytic activity in oxygen reduction, using "bare" silver particles as a control. Marked differences in ORR activity were observed and accounted for by the manipulation of the metal surface electronic structure, owing to unique metal–ligand interfacial bonding interactions that impacted the binding to reaction intermediates.

In the present study, a series of AuPd alloy nanoparticles were prepared through $NaBH_4$ reduction of metal-salt precursors with a deliberate variation of the initial feed ratio in the presence of 1-dodecyne by taking advantage of the strong affinity of alkyne ligands to transition-metal surfaces. With the alkyne capping ligands, the nanoparticles were stabilized under ambient conditions, readily dispersible in common organic solvents, and the size was controlled to within a narrow range. The structures of the resulting nanoparticles were then characterized by using a variety of microscopic and spectroscopic measurements. Electrochemical studies showed that the resulting nanoparticles all exhibited apparent electrocatalytic activity in the ORR, and the best performance was observed with the sample consisting of 91.2% Pd and 8.8% Au, where

the mass activity was over eight times better than that of commercial palladium black and the specific activity almost twice as good.

2. Results and Discussion

The chemical compositions of the AuPd alloy nanoparticles were first analyzed by performing XPS measurements. Figure 1 depicts the high-resolution scans of the Pd 3d and Au 4f electrons of the series of AuPd nanoparticles. It can be seen that
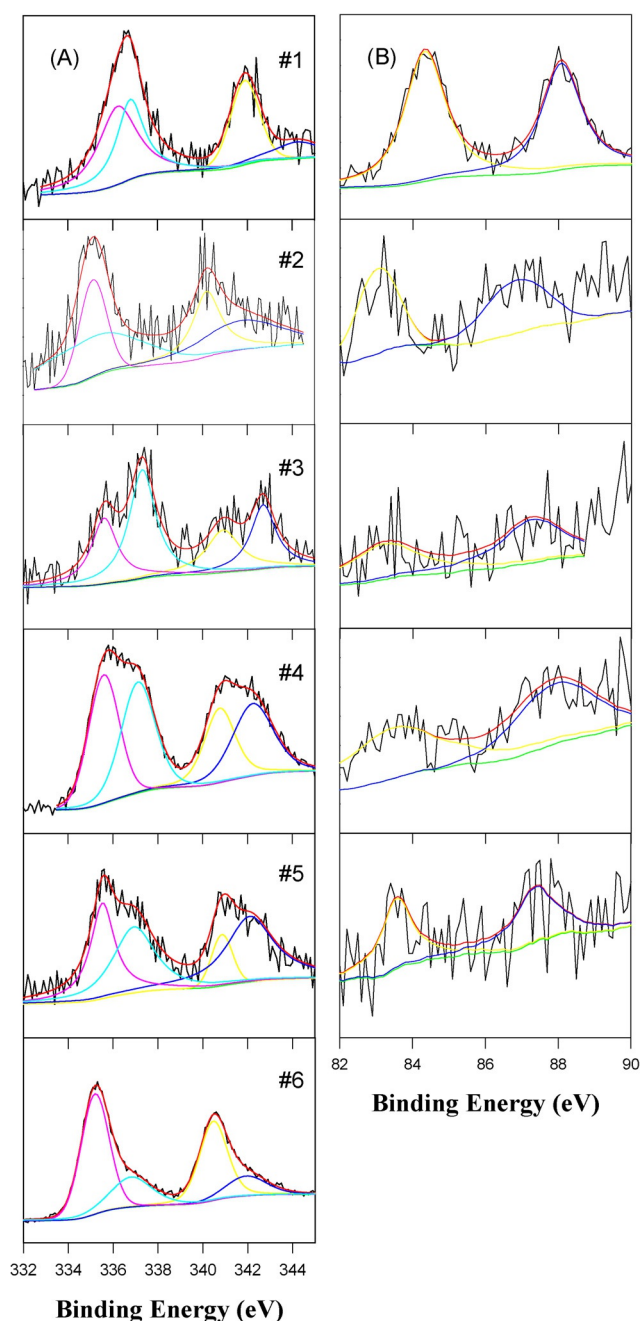

Figure 1. High-resolution XPS spectra of A) Pd 3d and B) Au 4f electrons of AuPd alloy nanoparticles at varied Pd concentrations of 64.9, 87.0, 91.2, 92.8, 94.1, and 100% for samples 1 to 6, repsectively. Black curves are experimental data and colored curves are deconvolution fits.

	Sample						Commercial
	1	2	3	4	5	6	Pd black
Core diameter [nm]	4.48 ± 0.51	3.12 ± 0.39	4.89 ± 0.60	2.68 ± 0.70	3.28 ± 0.83	4.11 ± 1.28	ca. 6.0 (Ref. [48])
Pd [at%]	64.9	87.0	91.2	92.8	94.1	100	100
Onset potential [V vs. RHE]	$+0.93$	$+0.97$	$+0.98$	$+0.98$	$+0.96$	$+0.96$	$+0.96$
J_s [μA cm^{-2}] at $+0.90$ V	158	110	610	245	204	253	356
J_m [A g^{-1}] at $+0.90$ V	39	64	162	95	41	30	19

Table 1. Summary of AuPd nanoparticle structure and ORR activity.

for all samples, the Pd 3d spectra may be deconvoluted into two doublets. The pairs at lower energies (335.6 and 340.9 eV) are consistent with those of metallic Pd, whereas those at somewhat higher energies (336.9 and 342.2 eV) may be assigned to Pd^{II} species.[38] This suggests the formation of a substantial amount of palladium oxide in the nanoparticles, which may, in part, be ascribed to electron transfer from palladium to gold as a result of the stronger electronegativity of gold than that of palladium. In contrast, for the Au 4f electrons, only a single pair of peaks may be resolved at approximately 83 and 87 eV, which are in good agreement with the binding energies of the $4f_{7/2}$ and $4f_{5/2}$ electrons of metallic Au, respectively.[38] The data are also listed in Table S1. Furthermore, based on the integrated peak areas, the atomic concentrations of palladium in the nanoparticle cores were estimated to be 64.9, 87.0, 91.2, 92.8, 94.1, and 100% for samples 1 to 6, respectively (Table 1).

Further structural insights were obtained by performing TEM measurements. Figure 2 shows a representative TEM image of the nanoparticles. One can see that the majority of the AuPd alloy nanoparticles were rather well dispersed without apparent aggregation, suggesting effective passivation of the metal cores by the alkyne ligands. In addition, statistical analysis based on more than 100 nanoparticles (Figure S1) shows that the average nanoparticle diameter actually fluctuated within the narrow range of 3–5 nm with palladium contents at 4.84 ± 0.51, 3.12 ± 0.39, 4.89 ± 0.60, 2.68 ± 0.70, 3.28 ± 0.83, and $4.11 \pm$

1.28 nm for samples 1 to 6, respectively. These data are also listed in Table 1. The slight variation in size is likely a result of the nanoparticle growth dynamics, where metal nucleation competes with ligand adsorption (nucleation vs. passivation).[39] That is, the bonding of alkyne ligands on Au is not as strong as on Pd and the reduction potential of Au^{III} ($+1.5$ V) is significantly more positive than that of Pd^{II} ($+0.987$), leading to different sizes for samples with different feeding ratios. Furthermore, well-defined lattice fringes can readily be identified for the AuPd nanoparticles from the high-resolution TEM images depicted in the corresponding figure insets. For samples with small percentages of gold (samples 3–6), the lattice spacing was in strong agreement with that of Pd(111) (2.24 Å). For the samples with a larger content of gold (samples 1 and 2), the lattice spacing was around 2.28 Å, which is in the intermediate range between those of Pd(111) and Au(111) (2.35 Å) crystalline planes, a common feature in bimetallic alloys.[27,34] This not only suggests alloying between the metals, but is also direct visual evidence of lattice strain in the nanoparticles.

UV/Vis absorption spectroscopy also confirmed the formation of nanosized particles, which was manifested by the exponential decay profiles, the so-called Mie scattering. From Figure 3 A, it can be seen that, for the sample exhibiting the highest concentration of gold (sample 1, 64.9% Pd and 35.1% Au) a broad peak centered around 520 nm also appeared, which was ascribed to the surface plasmon resonance of gold nanoparticles. The absence of this peak for samples with lower gold contents has previously been observed[34,36] and ascribed to the rearrangement of electron density between the two metals.[40]

FTIR measurements confirmed the bonding attachment of the dodecyne ligands on the metal nanoparticle surface. From Figure 3 B, one can see that, for monomeric ligands (black curve), several well-defined vibrational features can be readily identified, such as the terminal H—C$\equiv$ stretch at 3300 cm^{-1}, C$\equiv$C stretch at 2100 cm^{-1}, methyl and methylene stretches around 2900 cm^{-1}, and the scissoring and rocking of the carbon chains at 1470 and 1375 cm^{-1}, respectively. For the nanoparticle samples, however, the terminal H—C$\equiv$ stretch vanished altogether and the C$\equiv$C stretch red-shifted to 1846 cm^{-1} (Figure inset), whereas the rest of the vibrational features remained almost unchanged. This suggests the ready cleavage of the terminal H—C$\equiv$ bonds when the ligands self-assembled on the nanoparticle surface, forming metal–acetylide (M—C$\equiv$)/–vinylidene (M=C=CH—) interfacial bonds through a tautomeric rearrangement process and, hence, leading to a redshift of
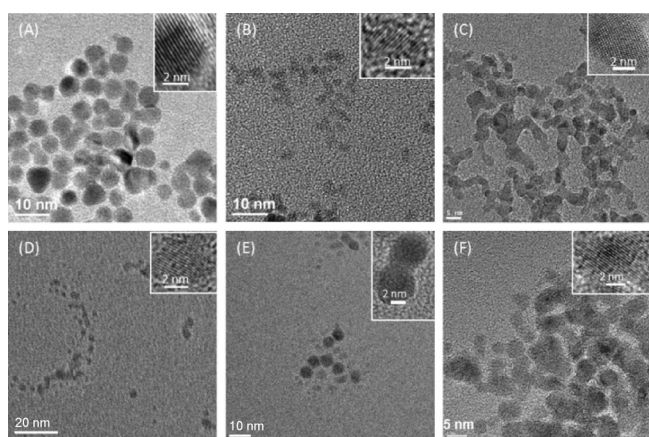

Figure 2. Representative TEM images of AuPdHC12 nanoparticles at different palladium concentrations: A) 64.9, B) 87.0, C) 91.2, D) 92.8, E) 94.1, and E) 100%. Insets show the corresponding high-resolution TEM images.
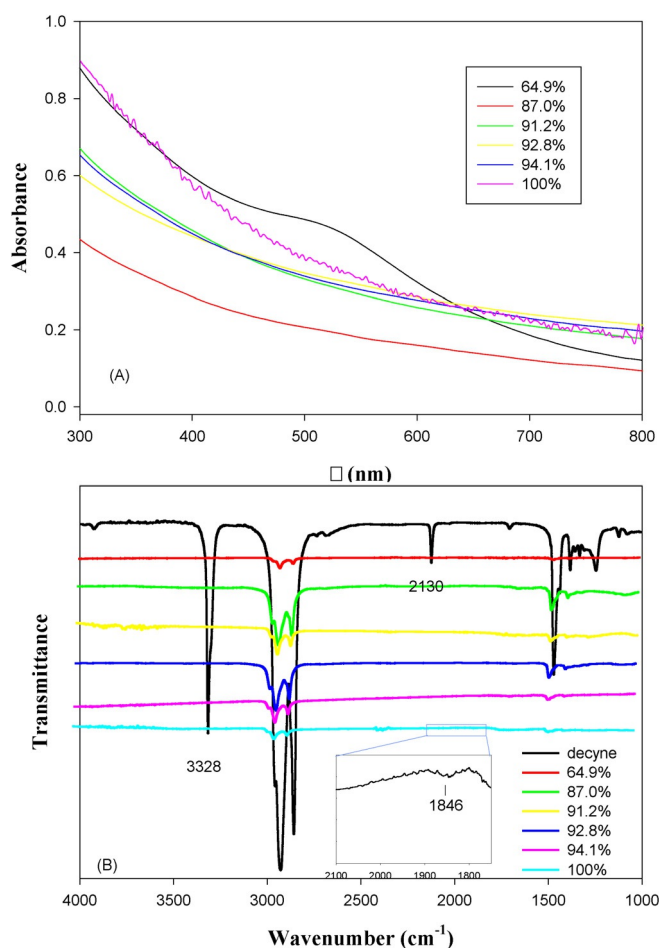
Figure 3. A) UV/Vis absorption spectra and B) FTIR spectra of 1-dododecyne-functionalized AuPd nanoparticles at various Pd concentrations. The FTIR spectrum of monomeric 1-dododecyne is also included as the black curve in panel (B). Inset shows the magnified region between 2100 and 1700 cm^{-1}.

Figure 4. Cyclic voltammograms of a glassy carbon electrode modified with different AuPd nanoparticles in nitrogen-saturated 0.1 M NaOH. The data for pure Au nanoparticles were also included as the aqua-blue curve. Potential sweep rate: 100 mV s^{-1}.

the C≡C stretch through intraparticle charge delocalization. Similar behaviors have been observed in a series of recent studies.[41–43] The absence of the H–C≡ vibrational stretch also signified that the nanoparticle samples were free of excessive monomeric ligands.

The electrocatalytic activity of the AuPd nanoparticles for the ORR was then examined and compared through voltammetric measurements in N$_2$- and O$_2$-saturated 0.1 M NaOH solutions. Note that, before the ORR measurements, the electrodes were subject to an electrochemical activation treatment by rapid potential cycling (500 mV s^{-1}) between 0 and +1.2 V (vs. RHE) in a N$_2$-saturated 0.1 M NaOH solution until a steady voltammogram was obtained. From Figure 4, it can be seen that, for pure gold nanoparticles (aqua blue curve) in N$_2$-saturated NaOH, the anodic scan of gold oxidation started to occur at about +1.15 V, whereas, in the cathodic scan, the reduction of gold oxide peaked at +0.991 V. In contrast, for pure palladium nanoparticles (magenta curve), the peak potential of the reduction of palladium oxide was far more negative at +0.567 V, indicating that palladium interacts far more strongly with oxygenated species than gold.[44] Interestingly, for the series of AuPd alloy nanoparticles, only a single cathodic peak was ob-
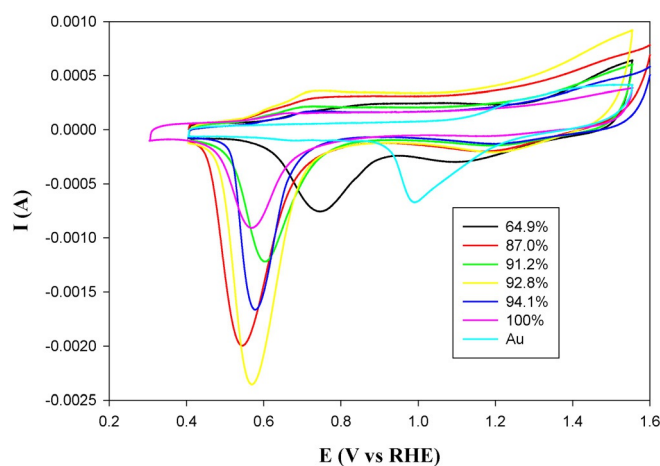
served, likely because of intimate alloying of the metals in the nanoparticles rather than formation of separate nanoparticles, as manifested in TEM measurements (Figure 2). In addition, the peak potential for metal-oxide reduction exhibited a clear variation with the elemental particle composition. For instance, for sample 1 (64.9% Pd), the oxide reduction peaked at +0.746 V, which is between those of pure Au and pure Pd, suggesting that both Pd and Au components were readily accessible on the nanoparticle surface; however, for other AuPd nanoparticles, the peak potentials were actually very close to that of pure Pd, at +0.546, +0.578, +0.568, and +0.604 V for samples 2 to 5, respectively. This implies that in these Pd-dominant nanoparticles (Pd concentrations >87%), the surface was primarily enriched with Pd.

In addition, based on the integrated peak area, the effective electrochemical surface area (ECSA) was estimated to be 18.0, 25.3, 15.3, 28.0, 14.7, and 10.7 m^{2}g^{-1} for samples 1 to 6, respectively. In comparison to the theoretical surface area (by assuming a spherical shape, Figure 2), the fraction of nanoparticle surface that was electrochemically accessible decreased roughly with increasing Pd concentration (20.8, 24.4, 12.8, 18.0, 7.9, and 7.4% for samples 1 to 6, respectively). This might be associated with the relatively strong bonding interactions of Pd with the alkyne ligands as compared to gold, such that an increase of Pd concentration in the nanoparticles would render it increasingly difficult to desorb the organic capping ligands during the electrochemical activation process.

The electrocatalytic activity for oxygen reduction was then evaluated by using rotating ring-disk electrode (RRDE) voltammetric measurements in O$_2$-saturated 0.1 M NaOH at different rotation rates. Figure 5 A depicts the RDE voltammograms of the series of AuPd nanoparticles at a rotation rate of 1600 RPM, along with that of commercial Pd black. It can be seen that nonzero currents started to appear at around +1.0 V and, at even more negative electrode potentials, the currents increased drastically and reached a plateau at potentials < +0.80 V. This signified apparent electrocatalytic activity of
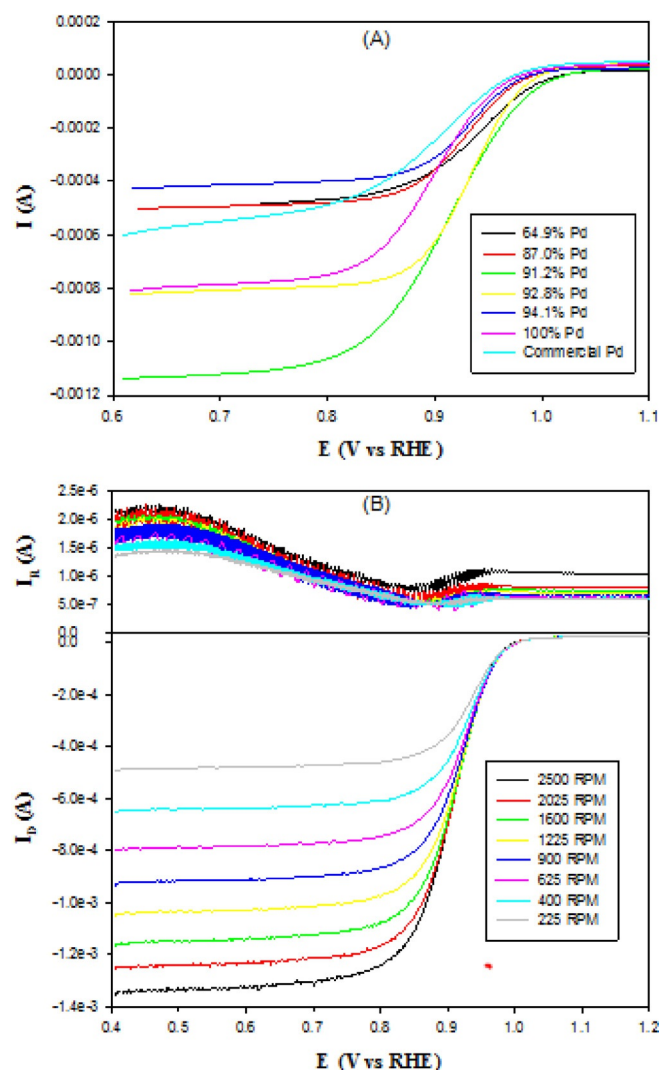
Figure 5. A) RRDE voltammograms of a glassy carbon electrode modified with various AuPd alloy nanoparticles in oxygen-saturated 0.1 M NaOH at 1600 RPM. B) RRDE voltammograms of a glassy carbon electrode modified with sample 3 AuPd alloy nanoparticles in oxygen-saturated 0.1 M NaOH. Disk potential sweep rate: 10 mV s^{-1}; ring potential: +1.5 V; catalyst loading: 0.60 g m^{-2}.

the nanoparticles in oxygen reduction. From the voltammograms, the onset potential of the ORR can be identified at +0.93, +0.97, +0.98, +0.98, +0.96, and +0.96 V for samples 1 to 6, respectively, and +0.96 V for Pd black. Of note is that the onset potentials of samples 3 and 4 were the most positive among the series, even slightly more positive (by up to 30 mV) than those of pure Pd nanoparticles (sample 6) and Pd black. In addition, the limiting currents also showed an apparent variation with the nanoparticle compositions. For instance, the limiting currents at +0.75 V were 0.48, 0.49, 1.10, 0.80, 0.41, and 0.78 mA for samples 1 to 6, respectively, and 0.53 mA for commercial Pd black (note that the metal loadings were the same for all nanoparticle catalysts). From these results, one can see that among the series, sample 3 (91.2% Pd) stood out as the best ORR catalyst with the most positive onset potential and highest limiting currents.

More detailed studies were carried out by using RRDE measurements. Figure 5 B depicts the RRDE voltammograms of AuPd nanoparticles (sample 3) at various electrode rotation rates (225–2500 RPM) with the ring potential set at +1.50 V. It can be seen that the disk limiting current increased with increasing electrode rotation rates, and the ring current was about two orders of magnitude lower than those at the disk electrode, signifying the production of only a minimal amount of peroxide species, such that the ORR most likely proceeded through the four-electron reduction pathway to OH$^-$. Similar behaviors are observed with other AuPd nanoparticles (Figure S2). In fact, based on the disk (I_D) and ring (I_R) currents, the electron-transfer number (n) can be quantitatively estimated by the equation, $n = 4I_D \big/ \left(I_{D+}{}^{I_R}\!/N \right)$, where N is collection efficiency of the electrode (40%).[15] Figure 6 depicts the variation
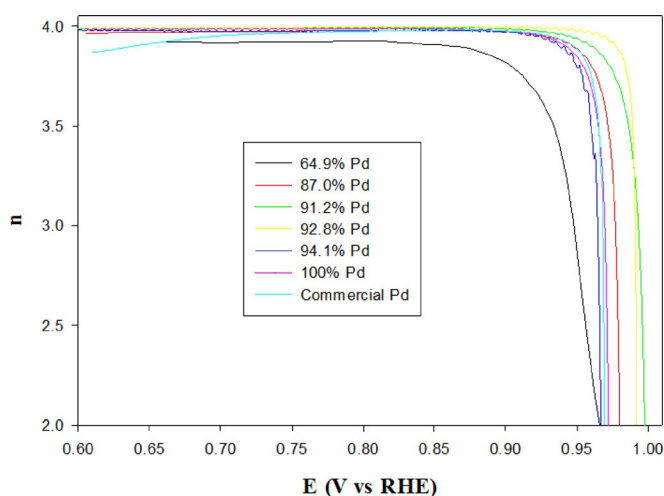

Figure 6. Variation in the electron transfer number of AuPd nanoparticles during oxygen reduction. Data were obtained from Figures 5 and S2.

of the n values with electrode potentials for the series of nanoparticle samples. It can be seen that, at potentials more negative than +0.90 V, all samples exhibited $n \approx 4.0$, except for sample 1 where $n \approx 3.92$, indeed suggesting almost full reduction of oxygen to OH$^-$.

The electron-transfer kinetics were further analyzed by using the Koutecky–Levich (K–L) method. As the voltammetric disk current (I_D) may include both kinetic (I_k) and diffusion-controlled (I_d) contributions, the K–L equation is expressed as shown in Equations (1)–(3):

$$\frac{1}{I_D} = \frac{1}{I_k} + \frac{1}{I_d} = \frac{1}{I_k} + \frac{1}{B\omega^{1/2}} \tag{1}$$

$$B = 0.62nFAC_O D_O^{2/3} v^{-1/6} \tag{2}$$

$$I_k = nAFkC_O \tag{3}$$

where ω is the electrode rotation rate, n is electron-transfer number, F is the Faraday constant (96485 C mol^{-1}), A is the geometric surface area of the electrode, C_O is the oxygen con-

centration in O_2-saturated solutions $(1.26\times10^{-6}\ \mathrm{mol\ cm}^{-3})$,[45] D_O is the diffusion coefficient of O_2 in 0.1 M NaOH aqueous solution $(1.93\times10^{-5}\ \mathrm{cm}^2\,\mathrm{s}^{-1})$,[46] v is the kinematic viscosity of the solution $(1.009\times10^{-2}\ \mathrm{cm}^2\,\mathrm{s}^{-1})$,[47] and k is the electron-transfer rate constant. As depicted in Figure S3, the K–L plots of I_D^{-1} versus $\omega^{-1}/2$ exhibited good linearity with consistent slopes in each sample, suggesting a first-order reaction with respect to oxygen concentration in the solution.

In addition, the y-axis intercepts of the linear regressions may be exploited for the quantification of the kinetic current density (J_k, I_k normalized to the ECSA of the nanoparticle catalysts). Figure 7A depicts the corresponding Tafel plot, where
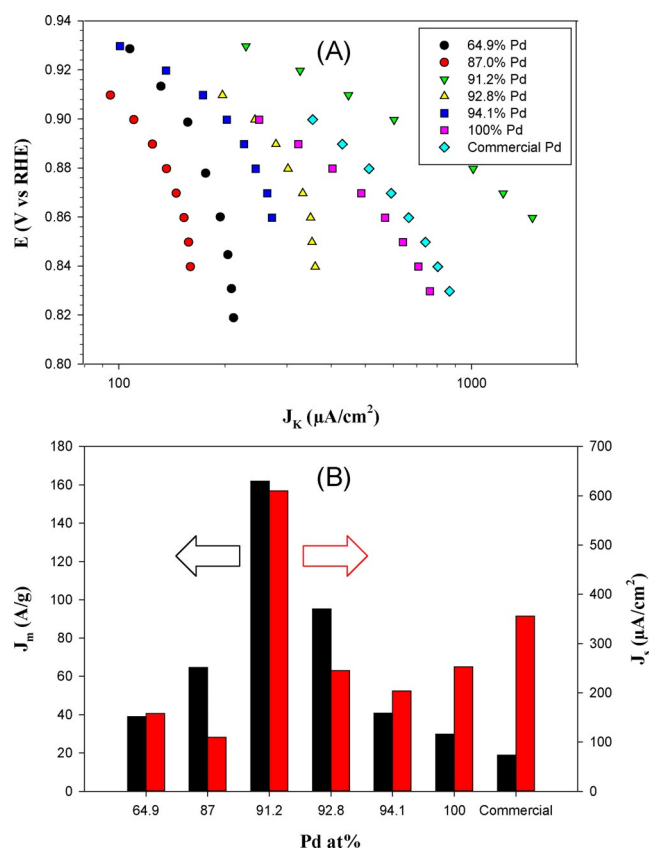

Figure 7. A) Tafel plot of dodecyne-capped AuPd nanoparticles in oxygen reduction. B) Comparison of the specific activity (J_s, red bars) and mass activity (J_m, black bars) at +0.90 V for the series of AuPd nanoparticles in ORR.

one can see that, for all samples, the kinetic current density increased markedly with increasingly negative electrode potential, and sample 3 (91.2 % Pd) stood out as the best catalyst among the series with the highest current density, even better than the commercial Pd black. For instance, at +0.90 V, the specific activity (J_k) was 158, 110, 610, 245, 204, and 253 $\mu\mathrm{A\,cm}^{-2}$ for samples 1 to 6, respectively, and 356 $\mu\mathrm{A\,cm}^{-2}$ for commercial Pd, as depicted by the red bars in panel B of Figure 7, where the activity of sample 3 was almost twice that of commercial Pd black. Similar behaviors can be observed with the mass activity (J_m, I_k normalized by the mass of the respective nanoparticles; black bars in panel B), which also ex-

hibited a volcano-shaped variation with Pd concentration in the nanoparticles (data also listed in Table 1). Again, sample 3 can be identified as the best catalyst among the series with a mass activity of about 162 $\mathrm{A\,g}^{-1}$, which was more than eight times that of a much larger commercial Pd black catalyst (ca. 6 nm in diameter)[48] and nearly five times that of dodecyne-capped pure palladium particles (sample 6).

It should be noted that, for the ORR, the Tafel slopes are typically found at 60 or 120 $\mathrm{mV\,dec}^{-1}$, where the former corresponds to a pseudo-two-electron reaction as the rate-determining step, and the latter suggests that the rate-determining step is a first-electron reduction of oxygen, implying that the subsequent reduction and O−O bond-breaking steps are relatively facile.[4] In the present study, linear regressions yielded Tafel slopes in the low overpotential regime ($E > +0.88$ V) of 181, 166, 69, 130, 85, 96 $\mathrm{mV\,dec}^{-1}$ for samples 1 to 6, respectively, and 125 $\mathrm{mV\,dec}^{-1}$ for commercial Pd. This seems to suggest that the ORR on sample 3 was largely limited by the pseudo-two-electron reduction step, whereas for samples 4 to 6 (high Pd loadings), the first-electron reduction was likely the rate-limiting step, similar to that of commercial Pd black. However, for samples 1 and 2 (low Pd loadings), the exceedingly high Tafel slopes suggest that oxygen adsorption was likely the limiting factor in the ORR kinetics, probably caused by the relatively high concentrations of gold that diminished the binding affinity to oxygen.

Note that the ORR performance of sample 3 is markedly better than leading results in the literature with relevant Pd-based alloy nanoparticles. For example, Sekol et al.[49] deposited silver–palladium core–shell alloy nanoparticles (diameter: 7.5 nm) onto multiwall carbon nanotubes and observed an onset potential of oxygen reduction around +0.9 V versus RHE and an n value of about 3. In another study, Hu et al.[50] decorated ordered mesoporous carbons with palladium–tungsten alloy nanoparticles that featured segregated nanoislands of palladium (ca. 1 nm) on the nanoparticle surface, and found that the onset potential of ORR was about +0.86 V versus RHE, a positive shift of 60 mV compared to that of ordered mesoporous carbons with tungsten nanoparticles alone. Alloy nanoparticles have also been prepared by incorporating Fe, Cu, and Ni into Pd at controlled concentrations through co-impregnation and single-phase colloidal methods, yielding stable particles on a Vulcan carbon support, and the best activities were found to be around 30 $\mathrm{A\,g}^{-1}$ for PdFe, 95 $\mathrm{A\,g}^{-1}$ for PdCu, and 20 $\mathrm{A\,g}^{-1}$ for PdNi at +0.90 V versus RHE.[51] Cobalt–palladium core–shell nanoparticles and alloy nanoparticles[52] have also been prepared and the onset potentials (+0.83 and +0.87 V) and specific activity (500 and 75 $\mu\mathrm{A\,cm}^{-2}$ at +0.75 V) remained subpar compared to those of the similarly sized AuPd alloy nanoparticles in the present study. In a recent study with oleylamine-functionalized Pd nanoparticles,[53] the specific activity of 100 $\mu\mathrm{A\,cm}^{-2}$ at +0.9 V was also markedly lower than the results in the present study.

Such a remarkable performance might be accounted for by gold alloying that led to diminished bonding interactions of the nanoparticles with oxygenated species,[20, 21] as compared to pure Pd. Note that in previous studies based on EXAFS

measurements,[25] it has been found that the palladium–oxygen bond might be suppressed with increasing gold content, leading to enhanced stabilization of surface palladium towards oxide-layer formation, as a result of possible charge transfer from palladium to gold, owing to the difference in electronic negativity, as suggested in XPS measurements (Figure 1). Additional contributions may arise from the alkyne capping ligands that form conjugated metal–ligand interfacial bonds, leading to extended spilling of metal core electrons into the ligand shells.[12, 54]

However, alloying may also produce lattice strain that has been found to shift the d-band center relative to the Fermi level and affect interactions with oxygenated intermediates.[3, 11] As evidenced in TEM measurements (Figure 2), the two metals are intimately mixed with a lattice spacing in between those of pure Pd and pure Au. That is, the incorporation of gold into the nanoparticles indeed led to the expansion of the Pd crystalline lattices, which raised the d-band center of Pd and enhanced the strength of the interaction between the nanoparticle and oxygen adsorbates. This was anticipated to result in decreasing catalytic activity.

Despite these two opposing effects, it is clear from the experimental results presented above that the ORR activity was enhanced with AuPd alloy nanoparticles, as compared to pure Pd. This indicates that electronic effects from the push-and-pull nature of heteroatoms (and deliberate surface engineering with the alkyne ligands) dominate the negative contributions from lattice strain. Furthermore, the volcano-shaped variation of the ORR performance with nanoparticle elemental composition suggests that, with the incorporation of an increasing amount of gold in the nanoparticles, binding to oxygen intermediates was likely weakened, leading to enhanced activity that reached a maximum with sample 3; a further increase in gold content resulted in interactions with oxygen intermediates that were too weak and diminished the ORR activity. This is a clear demonstration of Sabatier's postulate with the peak mass activity of sample 3 representing the optimal balance between these two opposing alloying effects.

3. Conclusions

A series of dodecyne-capped gold–palladium alloy nanoparticles of varying elemental compositions were readily prepared by using a simple chemical reduction route. XPS measurements showed that the palladium concentrations in the nanoparticle cores varied from 65 to 100 at % and the particle diameters were found to be mostly in the range of 2–6 nm, as manifested in TEM measurements. The formation of AuPd alloy nanoparticles was also observed in UV/Vis absorption measurements, and FTIR studies confirmed the successful self-assembly of the alkyne ligands onto the nanoparticle surface. Electrochemical studies showed that, for Pd-dominant nanoparticles, the reduction of metal oxides occurred at a potential similar to that of pure Pd, whereas at relatively high gold concentrations, the peak potential was actually in between those for pure Au and pure Pd. This suggests that alloying with gold indeed weakened the interactions of palladium with oxygen species.

In addition, all samples exhibited apparent electrocatalytic activity for the ORR in alkaline media, and the sample with 91.2 at % palladium exhibited the best performance, within the context of onset potential, electron transfer number, as well as mass and specific activity. In fact, the mass activity of this sample was more than eight times better than that of commercial palladium black, and almost twice as good in terms of specific activity. This is attributed to alterations of surface electronic properties as a result of interactions between gold and palladium atoms as well as unique metal–ligand bonding interactions with the alkyne ligands. This allows for optimum binding to oxygenated intermediates and enhanced electrocatalytic activity.

Experimental Section

Chemicals

Tetrachloroauric acid trihydrate (HAuCl$_4$·3H$_2$O, Acros), palladium chloride (PdCl$_2$, Acros), hydrochloric acid (HCl, certified ACS Plus, Fisher Scientific), tetra-*n*-octylammonium bromide (TOABr, 98%, Acros), 1-dodecyne (97%, Alpha Aesar), sodium borohydride (NaBH$_4$, 98%, Acros), Nafion 117 Solution (5%, Fluka), carbon black (XC-72R, Fuel Cell Store), palladium black (99.95%, Sigma Aldrich), and sodium bicarbonate (NaHCO$_3$, 99.7%, Fisher Scientific) were used as received. Solvents were purchased from typical commercial sources at their highest purity and used without further treatment. Water was supplied with a Barnstead Nanopure Water System (18.3 MΩ cm).

Nanoparticle Synthesis

The biphasic route towards the preparation of organically capped gold nanoparticles was adopted for the synthesis of dodecyne-capped AuPd alloy nanoparticles.[55] In a typical reaction, palladium chloride was first dissolved in concentrated HCl to prepare tetrachloropalladic acid (H$_2$PdCl$_4$), which was then mixed with tetrachloroauric acid (HAuCl$_4$) at a selected molar feed ratio (0.15 mmol in total) in 20 mL of water under magnetic stirring. The solution was then transferred into a 50 mL round-bottom flask, into which tetraoctylammonium bromide (0.45 mmol) dissolved in toluene was added, resulting in phase transfer of the metal complexes to the organic phase, as manifested by a clear aqueous layer in the bottom and the formation of a burgundy color in the top organic phase. The organic phase was then collected by using a separatory funnel and transferred to a round-bottom flask, into which 1-dodecyne (0.45 mmol) was then added. A freshly prepared solution of sodium borohydride (1.2 mmol) in chilled water was added dropwise into the solution under vigorous magnetic stirring. An immediate change of the solution color from burgundy to dark red/brown, depending on the relative content of palladium and gold, signified the formation of AuPd alloy nanoparticles. Water was then used to wash away residual salts with a separatory funnel, and rotary evaporation was used to condense the toluene layer to less than 0.5 mL. Addition of a large excess of methanol led to apparent precipitation of the nanoparticles from the solution, which were collected by centrifugation. The procedure was repeated several times to remove free ligands and other reaction byproducts. The resulting particles were soluble in nonpolar organic media such as CH$_2$Cl$_2$, THF, and toluene, and referred to as AuPdHC12. Six nanoparticle samples were prepared with the Pd atomic fraction

varied from approximately 65 to 100%, as determined by X-ray photoelectron spectroscopic (XPS) measurements (vide infra).

Spectroscopy

The nanoparticle size and morphological features were characterized with transmission electron microscopy (TEM, Philips CM300 at 300 kV). Alloy compositions and electronic structures were determined with XPS (PHI 5400/XPS instrument equipped with an AlKα source operated at 350 W and at 10^{-9} Torr). UV/Vis measurements were performed with an ATI Unicam AV4 spectrometer with a resolution of 2 nm. FTIR spectra were acquired with a PerkinElmer FTIR spectrometer (Spectrum one, spectral resolution 4 cm^{-1}) with samples loaded onto a ZnSe disk.

Electrochemistry

In a typical electrochemical test, AuPdHC12 nanoparticles were first dissolved in toluene at a concentration of 0.5 mg mL^{-1}. Carbon black was added to the amount of four times the mass of the metals (such that the metal loadings were approximately 20 wt%) and Nafion was added to the amount of 1/100 the volume of toluene. The electrocatalyst solution was then subject to sonication for 30 min to ensure proper dispersion. A RRDE with a glassy carbon disk and a gold ring was used as the working electrode, with an Ag/AgCl reference electrode and a platinum-sheet counter electrode. The Ag/AgCl reference was calibrated against a reversible hydrogen electrode (RHE) and the electrode potentials were reported with reference to this RHE in the study. Prior to catalyst deposition, the electrode was thoroughly polished with alumina slurry and then rinsed extensively with deionized water. The catalyst ink solution was then drop-cast onto the glassy carbon disk with a microliter syringe and allowed to completely dry before the application of dilute Nafion in ethanol. Electrochemical studies were carried out with a three-compartment electrochemical cell with the electrolyte solution (0.1 M NaOH) saturated with ultrahigh-purity N$_2$ or O$_2$ (Praxair).

Acknowledgements

[1] F. T. Wagner, B. Lakshmanan, M. F. Mathias, *J. Phys. Chem. Lett.* **2010**, *1*, 2204–2219.

[2] U. Cano-Castillo, *Rev. Mex. Fis.* **2013**, *59*, 85–92.

[3] I. E. L. Stephens, A. S. Bondarenko, U. Grønbjerg, J. Rossmeisl, I. Chorkendorff, *Energy Environ. Sci.* **2012**, *5*, 6744.

[4] C. Song, J. Zhang in *PEM Fuel Cell Electrocatalysis and Catalyst Layers: Fundamentals and Applications*, (Ed.: J. Zhang), Springer, London, **2008**, pp. 89–134.

[5] A. Rabis, P. Rodriguez, T. J. Schmidt, *ACS Catal.* **2012**, *2*, 864–890.

[6] J. K. Nørskov, J. Rossmeisl, A. Logadottir, L. Lindqvist, J. R. Kitchin, T. Bligaard, H. Jonsson, *J. Phys. Chem. B* **2004**, *108*, 17886–17892.

[7] H. A. Gasteiger, S. S. Kocha, B. Sompalli, F. T. Wagner, *Appl. Catal. B* **2005**, *56*, 9–35.

[8] S. Chen, H. A. Gasteiger, K. Hayakawa, T. Tada, Y. Shao-Horn, *J. Electrochem. Soc.* **2010**, *157*, A82–A97.

[9] D. C. Higgins, S. Y. Ye, S. Knights, Z. W. Chen, *Electrochem. Solid State Lett.* **2012**, *15*, B83–B85.

[10] J. R. Kitchin, J. K. Norskov, M. A. Barteau, J. G. Chen, *J. Chem. Phys.* **2004**, *120*, 10240–10246.

[11] P. Strasser, S. Koh, T. Anniyev, J. Greeley, K. More, C. Yu, Z. Liu, S. Kaya, D. Nordlund, H. Ogasawara, M. F. Toney, A. Nilsson, *Nat. Chem.* **2010**, *2*, 454–460.

[12] K. Liu, X. W. Kang, Z. Y. Zhou, Y. Song, L. J. Lee, D. Tian, S. W. Chen, *J. Electroanal. Chem.* **2013**, *688*, 143–150.

[13] G. Q. He, Y. Song, K. Liu, A. Walter, S. Chen, S. W. Chen, *ACS Catal.* **2013**, *3*, 831–838.

[14] Z. Y. Zhou, X. W. Kang, Y. Song, S. W. Chen, *J. Phys. Chem. C* **2012**, *116*, 10592–10598.

[15] Z. Y. Zhou, X. Kang, Y. Song, S. Chen, *Chem. Commun.* **2012**, *48*, 3391–3393.

[16] G. Q. He, Y. Song, B. Phebus, K. Liu, C. P. Deming, P. G. Hu, S. W. Chen, *Sci. Adv. Mater.* **2013**, *5*, 1727–1736.

[17] J. Greeley, I. E. L. Stephens, A. S. Bondarenko, T. P. Johansson, H. A. Hansen, T. F. Jaramillo, J. Rossmeisl, I. Chorkendorff, J. K. Nørskov, *Nat. Chem.* **2009**, *1*, 552.

[18] V. Tripković, E. Skúlason, S. Siahrostami, J. K. Nørskov, J. Rossmeisl, *Electrochim. Acta* **2010**, *55*, 7975–7981.

[19] V. R. Stamenkovic, B. Fowler, B. S. Mun, G. Wang, P. N. Ross, C. A. Lucas, N. M. Markovic, *Science* **2007**, *315*, 493–497.

[20] A. Damjanovic, V. Brusic, J. O. Bockris, *J. Phys. Chem.* **1967**, *71*, 2741–2742.

[21] A. Damjanovic, V. Brusic, *Electrochim. Acta* **1967**, *12*, 1171–1184.

[22] I. E. Stephens, A. S. Bondarenko, F. J. Perez-Alonso, F. Calle-Vallejo, L. Bech, T. P. Johansson, A. K. Jepsen, R. Frydendal, B. P. Knudsen, J. Rossmeisl, I. Chorkendorff, *J. Am. Chem. Soc.* **2011**, *133*, 5485–5491.

[23] P. Sabatier, *Ber. Dtsch. Chem. Ges.* **1911**, *44*, 1984–2001.

[24] M. Nie, P. K. Shen, Z. Wei, *J. Power Sources* **2007**, *167*, 69–73.

[25] C. Koenigsmann, E. Sutter, R. R. Adzic, S. S. Wong, *J. Phys. Chem. C* **2012**, *116*, 15297–15306.

[26] M. M. Maye, N. N. Kariuki, J. Luo, L. Han, P. Njoki, L. Y. Wang, Y. Lin, H. R. Naslund, C. J. Zhong, *Gold Bull.* **2004**, *37*, 217.

[27] O. Metin, X. L. Sun, S. H. Sun, *Nanoscale* **2013**, *5*, 910–912.

[28] A. Jabloński, S. H. Overbury, G. A. Somorjai, *Surf. Sci.* **1977**, *65*, 578–592.

[29] J. H. Kim, W. W. Bryan, H. W. Chung, C. Y. Park, A. J. Jacobson, T. R. Lee, *ACS Appl. Mater. Interfaces* **2009**, *1*, 1063–1069.

[30] N. Dimitratos, J. A. Lopez-Sanchez, S. Meenakshisundaram, J. M. Anthonykutty, G. Brett, A. F. Carley, S. H. Taylor, D. W. Knight, G. J. Hutchings, *Green Chem.* **2009**, *11*, 1209–1216.

[31] J. H. Jiang, A. Kucernak, *Electrochim. Acta* **2009**, *54*, 4545–4551.

[32] A. N. Simonov, P. E. Plyusnin, Y. V. Shubin, R. I. Kvon, S. V. Korenev, V. N. Parmon, *Electrochim. Acta* **2012**, *76*, 344–353.

[33] P. Paalanen, B. M. Weckhuysen, M. Sankar, *Catal. Sci. Technol.* **2013**, *3*, 2869.

[34] S. Devarajan, P. Bera, S. Sampath, *J. Colloid Interface Sci.* **2005**, *290*, 117–129.

[35] X. Yuan, G. Sun, H. Asakura, T. Tanaka, X. Chen, Y. Yuan, G. Laurenczy, Y. Kou, P. J. Dyson, N. Yan, *Chemistry* **2013**, *19*, 1227–1234.

[36] G. Zhang, H. Zhou, C. An, D. Liu, Z. Huang, Y. Kuang, *Colloid Polym. Sci.* **2012**, *290*, 1435–1441.

[37] H. F. Liu, G. P. Mao, S. J. Meng, *J. Mol. Catal.* **1992**, *74*, 275–284.

[38] C. D. Wagner, W. M. Riggs, L. E. Davis, J. F. Moulder, G. E. Muilenberg, *Handbook of x-ray photoelectron spectroscopy : a reference book of standard data for use in x-ray photoelectron spectroscopy*, PerkinElmer Corp., Eden Prairie, MN, **1979**.

[39] S. Chen, A. C. Templeton, R. W. Murray, *Langmuir* **2000**, *16*, 3543–3548.

[40] J. A. Creighton, D. G. Eadon, *J. Chem. Soc. Faraday Trans.* **1991**, *87*, 3881–3891.

[41] W. Chen, N. B. Zuckerman, X. W. Kang, D. Ghosh, J. P. Konopelski, S. W. Chen, *J. Phys. Chem. C* **2010**, *114*, 18146–18152.

[42] X. W. Kang, N. B. Zuckerman, J. P. Konopelski, S. W. Chen, *Angew. Chem. Int. Ed.* **2010**, *49*, 9496–9499; *Angew. Chem.* **2010**, *122*, 9686–9689.

[43] X. W. Kang, N. B. Zuckerman, J. P. Konopelski, S. W. Chen, *J. Am. Chem. Soc.* **2012**, *134*, 1412 – 1415.

[44] C. H. Lin, C. H. Lee, J. H. Chao, C. Y. Kuo, Y. C. Cheng, W. N. Huang, H. W. Chang, Y. M. Huang, M. K. Shih, *Catal. Lett.* **2004**, *98*, 61 – 66.

[45] A. Schumpe, I. Adler, W. D. Deckwer, *Biotechnol. Bioeng.* **1978**, *20*, 145 – 150.

[46] N. A. Anastasijević, Z. M. Dimitrijevic, R. R. Adzic, *Electrochim. Acta* **1986**, *31*, 1125 – 1130.

[47] N. M. Marković, H. A. Gasteiger, B. N. Grgur, P. N. Ross, *J. Electroanal. Chem.* **1999**, *467*, 157 – 163.

[48] R. C. Cerritos, M. Guerra-Balcázar, R. F. Ramírez, J. Ledesma-García, L. G. Arriaga, *Materials* **2012**, *5*, 1686 – 1697.

[49] R. C. Sekol, X. Li, P. Cohen, G. Doubek, M. Carmo, A. D. Taylor, *Appl. Catal. B* **2013**, *138*, 285 – 293.

[50] G. Hu, F. Nitze, E. Gracia-Espino, J. Ma, H. R. Barzegar, T. Sharifi, X. Jia, A. Shchukarev, L. Lu, C. Ma, G. Yang, T. Wagberg, *Nat. Commun.* **2014**, *5*, 5253.

[51] X. Wang, N. Kariuki, S. Niyogi, M. Smith, D. J. Myers, T. Hofmann, Y. Zhang, M. Bar, C. Heske, *Ecs Trans.* **2008**, *16*, 109 – 119.

[52] J. H. Jang, C. Pak, Y. U. Kwon, *J. Power Sources* **2012**, *201*, 179 – 183.

[53] Y. Shi, S. Yin, Y. Ma, D. Lu, Y. Chen, Y. Tang, T. Lu, *J. Power Sources* **2014**, *246*, 356 – 360.

[54] K. Liu, Y. Song, S. W. Chen, *J. Power Sources* **2014**, *268*, 469 – 475.

[55] M. Brust, M. Walker, D. Bethell, D. J. Schiffrin, R. Whyman, *J. Chem. Soc. Chem. Commun.* **1994**, *801*, 802.